ARMY RESEARCH LABORATORY

ARL

Demonstration of Shear Localization in Ultrafine Grained Tungsten Alloys via Powder Metallurgy Processing Route

by Brady Butler, Eric Klier, Daniel Casem, Ajmer Dwivedi, Micah Gallagher, and Judy Hays

NOTICES

Disclaimers

The findings in this report are not to be construed as an official Department of the Army position unless so designated by other authorized documents.

Citation of manufacturer's or trade names does not constitute an official endorsement or approval of the use thereof.

Destroy this report when it is no longer needed. Do not return it to the originator.

Army Research Laboratory
Aberdeen Proving Ground, MD 21005-5069

Demonstration of Shear Localization in Ultrafine Grained Tungsten Alloys via Powder Metallurgy Processing Route

Brady Butler, Eric Klier, and Daniel Casem
Weapons and Materials Research Directorate, ARL

Ajmer Dwivedi
Dynamic Sciences Inc.

Micah Gallagher and Judy Hays
Bowhead Science and Technology, LLC

REPORT DOCUMENTATION PAGE			Form Approved OMB No. 0704-0188
Public reporting burden for this collection of information is estimated to average 1 hour per response, including the time for reviewing instructions, searching existing data sources, gathering and maintaining the data needed, and completing and reviewing the collection information. Send comments regarding this burden estimate or any other aspect of this collection of information, including suggestions for reducing the burden, to Department of Defense, Washington Headquarters Services, Directorate for Information Operations and Reports (0704-0188), 1215 Jefferson Davis Highway, Suite 1204, Arlington, VA 22202-4302. Respondents should be aware that notwithstanding any other provision of law, no person shall be subject to any penalty for failing to comply with a collection of information if it does not display a currently valid OMB control number. **PLEASE DO NOT RETURN YOUR FORM TO THE ABOVE ADDRESS.**			
1. REPORT DATE (DD-MM-YYYY) September 2012	**2. REPORT TYPE** Final		**3. DATES COVERED** (From - To) 18 July 2012
4. TITLE AND SUBTITLE Demonstration of Shear Localization in Ultrafine Grained Tungsten Alloys via Powder Metallurgy Processing Route			**5a. CONTRACT NUMBER**
			5b. GRANT NUMBER
			5c. PROGRAM ELEMENT NUMBER
6. AUTHOR(S) Brady Butler, Eric Klier, Daniel Casem, Ajmer Dwivedi[*], Micah Gallagher[**], and Judy Hays[**]			**5d. PROJECT NUMBER**
			5e. TASK NUMBER
			5f. WORK UNIT NUMBER
7. PERFORMING ORGANIZATION NAME(S) AND ADDRESS(ES) U.S. Army Research Laboratory ATTN: RDRL-WMM-F Aberdeen Proving Ground, MD 21005-5069			**8. PERFORMING ORGANIZATION REPORT NUMBER** ARL-TR-6214
9. SPONSORING/MONITORING AGENCY NAME(S) AND ADDRESS(ES)			**10. SPONSOR/MONITOR'S ACRONYM(S)**
			11. SPONSOR/MONITOR'S REPORT NUMBER(S)
12. DISTRIBUTION/AVAILABILITY STATEMENT Approved for public release; distribution is unlimited.			
13. SUPPLEMENTARY NOTES [*]Dynamic Sciences Inc., [**]Bowhead Science and Technology, LLC			

14. ABSTRACT

Mechanical properties and deformation characteristics are very closely linked to the underlying microstructure of a material. As the grain size of a metal is pushed to ultrafine (<1000 nm) and nano (<100 nm) length-scales, there is often a fundamental shift in the deformation mechanisms of these materials. In particular, tungsten and tungsten alloys have been shown to deform by shear localization as opposed to stable plastic flow when their grain size approaches 100 nm. While this failure mechanism is not ideal for many structural applications, it does provide an opportunity for improving the ballistic performance of tungsten in kinetic energy penetrator applications. This report analyzes the deformation characteristics of bulk, ultrafine grained tungsten and tungsten alloys produced via a powder metallurgy. In addition to grain size, the ability to shear localize is a strongly dependent on the overall ductility of the material. This research represents the first bulk demonstration of shear localization in a high density (>18 cm^3) tungsten based alloy tested in the as-sintered state.

15. SUBJECT TERMS

tungsten, shear localization, kinetic energy penetrator, depleted uranium replacement

16. SECURITY CLASSIFICATION OF:			**17. LIMITATION OF ABSTRACT**	**18. NUMBER OF PAGES**	**19a. NAME OF RESPONSIBLE PERSON** Brady Butler
a. REPORT Unclassified	**b. ABSTRACT** Unclassified	**c. THIS PAGE** Unclassified	UU	36	**19b. TELEPHONE NUMBER** (Include area code) 410-306-0835

Standard Form 298 (Rev. 8/98)
Prescribed by ANSI Std. Z39.18

Contents

List of Figures

List of Tables

Acknowledgments

INTENTIONALLY LEFT BLANK.

1. Introduction

Tungsten based alloys have received significant attention as a potential material to replace depleted uranium (DU) in kinetic energy penetrator (KEP) applications. While conventional tungsten alloys have proven to be a viable alternative to DU with respect to density, strength, and cost, the deformation properties at ballistic strain rates have become an inhibiting factor for fielding tungsten as a material for DU replacement. The research of Magness (*1–3*) has shown that conventional tungsten and its alloys undergo stable plastic flow at ballistic strain rates, which causes the material to "mushroom" when interacting with the target. On the other hand, DU materials that are typically used in KEP applications achieve unstable deformation at ballistic rates through the formation of adiabatic shear bands (ASB.) This shear localization causes the head of the penetrator to slough off early in the deformation event leading to a "self sharpening" behavior. This deformation instability ultimately results in a narrower channel and deeper penetration upon interacting with the target.

There have been many attempts to create the deformation instability exhibited in ASB in tungsten and its alloys through the use of highly oriented structures (*4, 5*) and bulk metallic glasses (*6*). However, each of these materials has a penalty with regard to density or performance when compared with DU. Research has indicated that ultrafine grained (UFG) materials may demonstrate shear localization regardless of the deformation properties of their coarse grained counterparts (*7, 8*). The shear localization that occurs in UFG materials will occur regardless of the deformation rate indicating that this deformation mechanism is non-adiabatic in nature as opposed to the adiabatic mechanism that is observed in DU based KEPs (*9*); however, this should result in the same performance increase in ballistic events. This discovery of grain size affecting the propensity for shear localization has spurred significant research into the development of UFG tungsten and tungsten alloys to achieve the deformation modes necessary to match DU's ballistic performance.

Studies by Wei et. al (*10–12*) have indicated that pure tungsten is capable of achieving shear localization at high strain rates when processed via a "top-down" severe plastic deformation route. These samples showed localization as the grain size approached 100 nm though the microstructure was heavily textured as a result of the high pressure torsion (HPT) processing route (*13, 14*). While this demonstration of shear localization implies that tungsten may be able to achieve DU performance, these materials have never been tested in a ballistic event as a result of the small sample sizes and geometries that result from HPT and are incompatible with ballistic testing.

Powder metallurgy processing routes have shown a strong potential for creating UFG tungsten alloys that are capable of achieving the dimensions necessary for ballistic testing; however, the sintering of nanocrystalline powders typically causes significant grain growth during

densification, resulting in coarse grained microstructures or residual porosity in the final structure. Recent research at the U.S. Army Research Laboratory (ARL) has demonstrated that these nanocrystalline powders may be able to achieve some degree of thermal stability through the use of kinetic pinning agents (*15*). This advent allows for the production of highly dense structures (90%–95% of theoretical density) with minimal grain growth resulting in a bulk, UFG microstructure (100–400-nm grain size).

While these materials exhibit very high strengths and densities, residual porosity and a lack of deformation processing creates inherently brittle tungsten that is prone to fracture along grain boundaries. These materials typically exhibit a ductile to brittle transition temperature (DBTT) that is higher than room temperature and are therefore unsuitable for ballistic applications. While thermomechanical processing of tungsten has proven effective for ductilizing conventional tungsten for the past 100 years (*16*) the fine microstructure and incredibly fine, well dispersed porosity of this ultrafine tungsten typically results in brittle fracture even at temperatures as high as 1300 °C leading to research into alternative methods for ductilization. Rhenium has been proven very effective in reducing the DBTT of tungsten when forming a solid solution. However, there is still some debate as to whether this enhanced ductility is a result of improved dislocation mobility (*17, 18*) or an increased solubility for interstitial elements (*19, 20*) that tend to embrittle grain boundaries. Also, boron has demonstrated its effectiveness in reducing the DBTT, albeit to a lesser extent than rhenium, by improving grain boundary cohesion (*21, 22*). A more general technique for ductilizing nanocrystalline materials has been developed by Wang et. al (*23*). The creation of a bi-modal microstructure can improve ductility without sacrificing much of the mechanical properties driven by the nanograined phase. Each ductilization technique was applied to create UFG tungsten based alloys that are suitable for testing in the as-sintered state. The goal of this research was to outline the requirements for demonstrating shear localization in as-sintered powder metallurgy samples of various compositions. Alloy compositions were chosen to enhance the room temperature ductility of the test specimens.

2. Experimental

Six tungsten alloy samples with immersion densities varying between 17.79 and 18.64 cm^3, were selected for quasi-static and dynamic compression tests. Each sample had an UFG tungsten microstructure but varied in composition depending on alloying additions. The six compositions chosen were: nominally pure nano-tungsten (nW), nano-tungsten with 0.075 weight-percent boron (nW-B), a bi-modal grain size of nano and 4-µm coarse grained tungsten (nW-Bi Modal) and nano-tungsten alloys with 5, 10, and 25 weight-percent rhenium (nW-5Re, nW-10Re, and nW-25Re) respectively. While processing parameters were designed to avoid significant

microstructural differences between samples, process variability and variations in chemical composition ultimately resulted in microstructural defects and microcracking in some specimens. Mechanical test specimens (2-mm cubes) were cut from each sample group by electrical discharge machining (EDM) and subsequently polished to a 1-µm finish on a diamond lapping wheel. Some specimens were tested in the as-EDM state to provide evidence for comparison of surface finish.

Low strain-rate ($\sim 1 \times 10^{-3}$/s) compression experiments were performed with an Instron model no. 1331 servo-hydraulic load frame with a 5000 lb (22.2 kN) load cell attached to measure force. Specimen deformation was measured using a linear variable differential transformer to measure cross-head displacement with a correction to adjust for machine compliance. Specimens were loaded between polished WC platens, which remained elastic during each experiment. Interfaces between the specimen and platens were lubricated with molybdenum disulfide (MoS_2) grease to reduce the effects of friction. All experiments were performed at room temperature.

High rate compression experiments ($\sim 10^3$ to 10^4/s) were performed with a 9.5-mm diameter Vascomax C350 steel Split Hopkinson Bar (SHB) (24). UFG tungsten tends to behave in a brittle manner, so small copper pulse shapers were used to ramp the incident pulse and obtain better data over what is essentially linear elastic loading to failure. As with the low-rate experiments, WC platens lubricated with MoS_2 paste were used on the loading interface of each test sample. The platens are impedance matched to the pressure bars to minimize the effects of wave propagation. All data analysis includes corrections for bar wave dispersion (25, 26). A DRS Hadland Imacon 200 high-speed digital camera was used in some of the high-rate experiments to obtain images of the deforming specimens.

After testing, samples were imaged using an Olympus OSL300 confocal microscope. Samples were also sectioned, mounted, polished, and evaluated using a Hitachi 4700 or FEI Nano600, high resolution scanning electron microscope (HRSEM). Grain size was determined by linear intercept method analysis and backscatter electron (BSE) scanning electron microscope (SEM) images were taken to enhance orientation contrast between grains. Hardness values were acquired using a Clark CM 400AT Vickers microhardness indenter with a 500-g load. Hardness indents were subjected to further evaluation in the confocal microscope as additional evidence of shear localization behavior. A Panalytical MRD Pro system was used to perform x-ray diffraction (XRD) analysis on sintered samples to identify phase segregation for selected compositions.

3. Results

3.1 Microstructure

The microstructural characteristics of each sample varied considerably as a result of composition and variability in the milling and sintering conditions for each material. While each sample invariably showed an UFG microstructure, there were significant differences with respect to the average grain size and residual porosity in each sample. The BSE SEM micrographs of each sample are shown in figures 1 and 2.
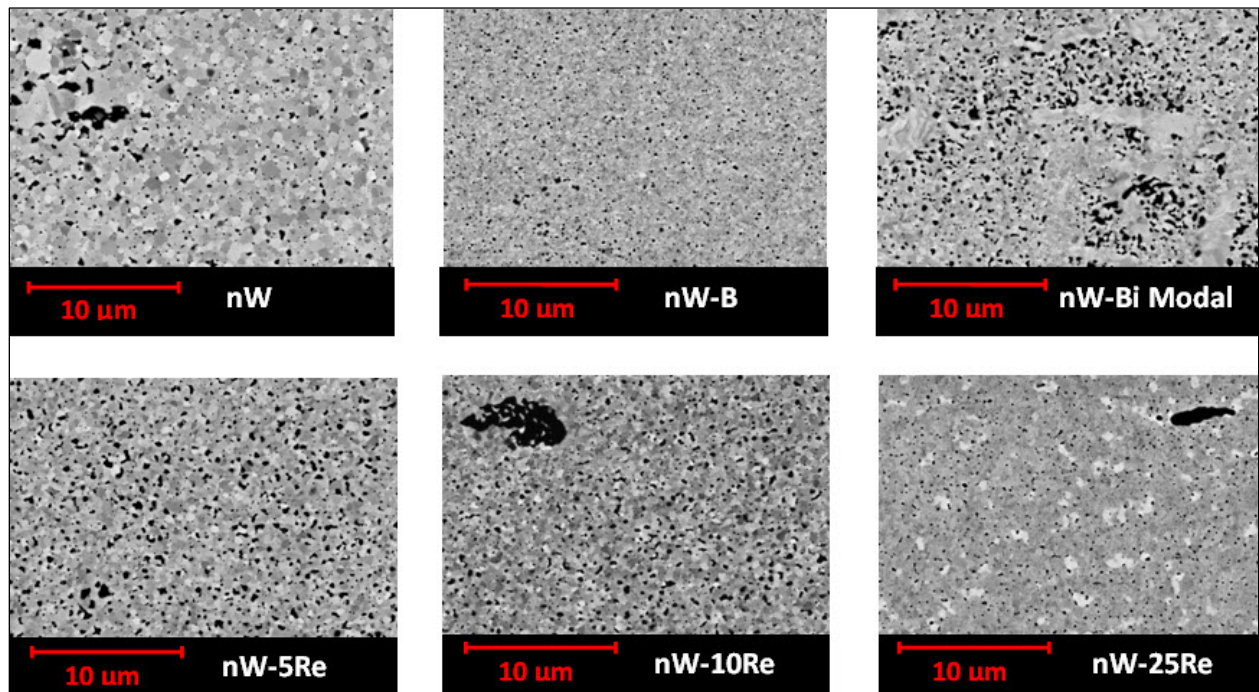

Figure 1. BSE micrographs showing the microstructure of UFG tungsten samples subjected to shear localization tests.
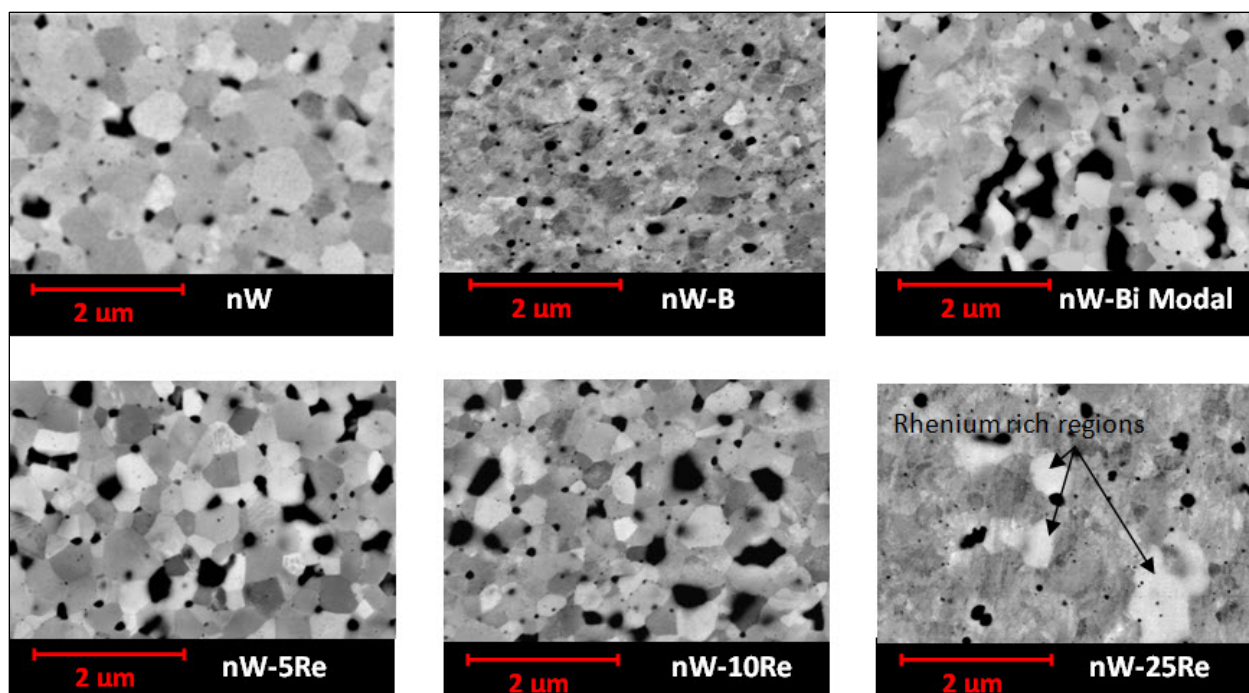
Figure 2. BSE micrographs showing the microstructure of UFG tungsten samples subjected to shear localization tests.

While there is a significant difference in the grain size and morphology between samples, there is no clear distinction between microstructures concerning their tendency to localize in a high strain rate event. In the nominally pure nano-tungsten sample, the micrographs show a fairly large grain size compared to the other samples. Lower magnification images clearly show the presence of large regions with contiguous porosity that should be detrimental to achieving a high degree of ductility. The W-B sample shows an extremely fine grain size with very fine and uniform porosity. While microcracking was not observed in these micrographs, some cracking was observed on the polished surfaces of compression test specimens, which may have resulted from the sintering process. The bi-modal tungsten sample shows elongated, coarse grains evenly distributed throughout the sample with no discernible orientation preference for the coarse grains. Fine porosity is distributed throughout the sample, but large porous regions are concentrated around the coarse tungsten grains. This microstructural defect may reduce the effectiveness of this coarse ductilizing phase. Each of the tungsten rhenium samples show a uniform UFG microstructure ranging between 200 and 350 nm. Unfortunately, the 25% rhenium sample also shows some segregation between the tungsten and rhenium phases as a result of incomplete mechanical alloying, indicated by bright rhenium-rich regions in the BSE micrographs. This type of segregation is usually detrimental to the material properties of tungsten-rhenium alloys as it reduces the local concentration of rhenium in solution and may result in the formation of a brittle σ phase (WRe) intermetallic. This intermetallic compound was detected by XRD in the nW-25Re sample, but this was not observed in any of the other rhenium containing samples.

3.2 Hardness

Vickers microhardness tests were performed to determine the hardness of the material. Indents were analyzed to determine basic information regarding the deformation behavior. Nanomaterials exhibit "pile ups" at the edge of the indents on the specimen as a result of the shear localization process that occurs at fine grain sizes indicating a transition to amorphous, glass-type deformation behavior (27). While this pile-up effect is an effective demonstration that the material could localize under very specific loading conditions, it does not demonstrate that the material has the ductility to achieve this unstable deformation mode without fracture. Cracking was not observed around any of the hardness indents. Optical micrographs of edge regions in microhardness indents are shown in figure 3.
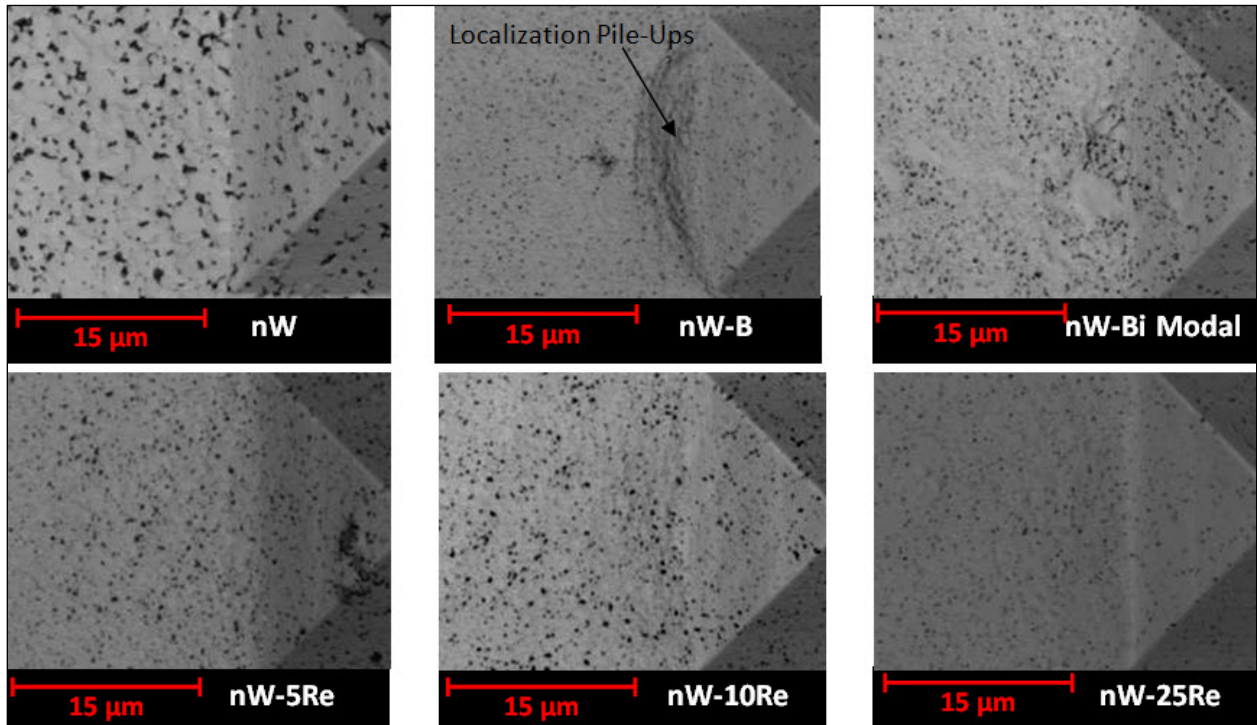
Figure 3. Optical micrographs of hardness deformation region adjacent to hardness indent. Pile-ups appear smooth and homogeneous in each of the samples except for the nW-B material, which shows small ledges indicative of localization.

Depth profile images were also taken with the confocal microscope to analyze variations in the height of pile-ups for each specimen. The pile up height was determined by averaging the deflection of the pile up region from the surface of the sample on all four sides of the indent. Results for the depth profile imaging are shown in figure 4.
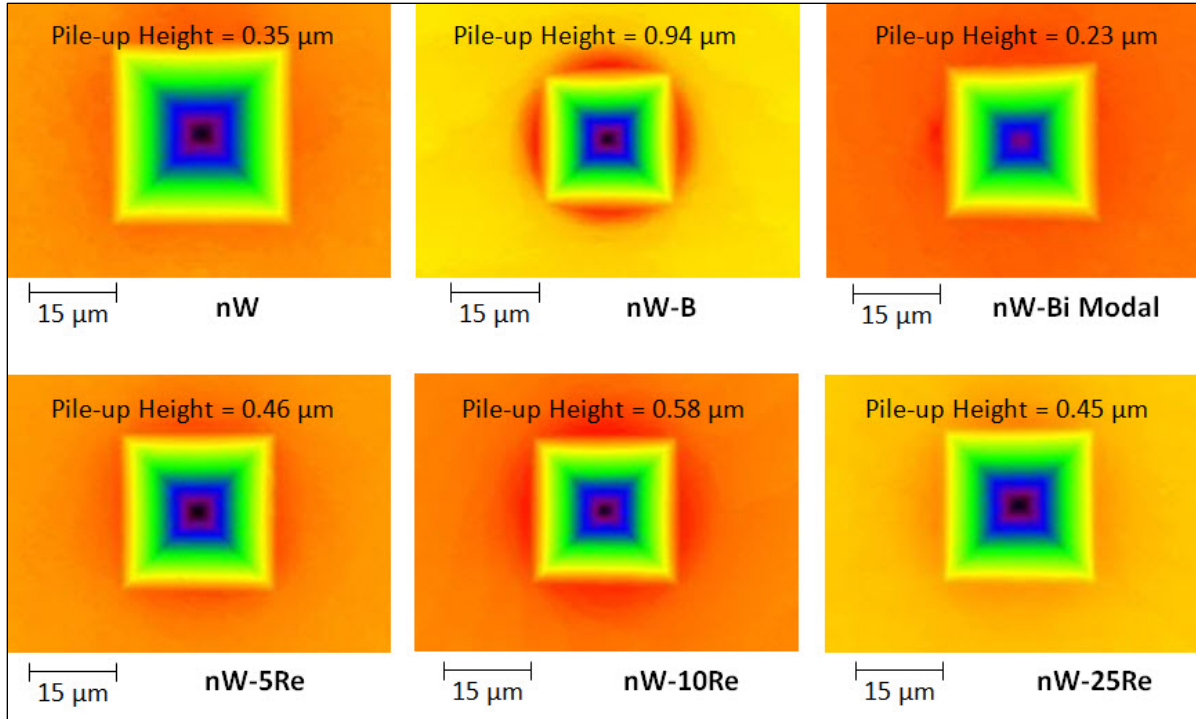
Figure 4. Topographic confocal images of hardness indents showing the relative height of the specimen as a function of color.

Although there are a number of factors that influence the height of a pile-up around a microhardness indent (geometry of indenter, residual porosity, size and depth of indent, etc.) the height of a pile-up can help to indicate the extent of localized deformation within the surface of the sample. The hardness indents shown in figures 3 and 4 indicate that each sample exhibits some degree of pile-up around the flat edge of the indent. However, only the nW-B sample shows the obvious ridges that are characteristic of shear localization in the pile up region. Furthermore, the height of the pile-up region in the nW-B sample is nearly double that of all other samples tested. The lowest recorded pile-up height, indicative of homogeneous plastic deformation, was recorded in samples with the two largest grain sizes.

### 3.3 Mechanical Testing and Post Mortem Analysis

Compression testing was performed on each of the nano-tungsten compositions. A minimum of two samples of each composition were tested in quasi-static and dynamic compression tests; however, the nW-B samples failed very early in quasi-static testing and only dynamic compression curves are shown for that specimen. The nW-B sample exhibited the highest strength of any material while the nW-25Re sample demonstrated the highest ductility without cracking. All of the rhenium containing samples showed sufficient ductility to survive testing without catastrophic failure and demonstrated shear localization in both high and low rate compression tests. All other compositions fractured in a brittle fashion before any significant degree of plasticity was recorded. Stress-strain compression curves are shown for each of the

samples tested and post-mortem imaging was performed whenever a significantly large portion of the sample remained after testing. Each of the post mortem images was taken with the loading direction aligned horizontal to the image as shown in figure 5.
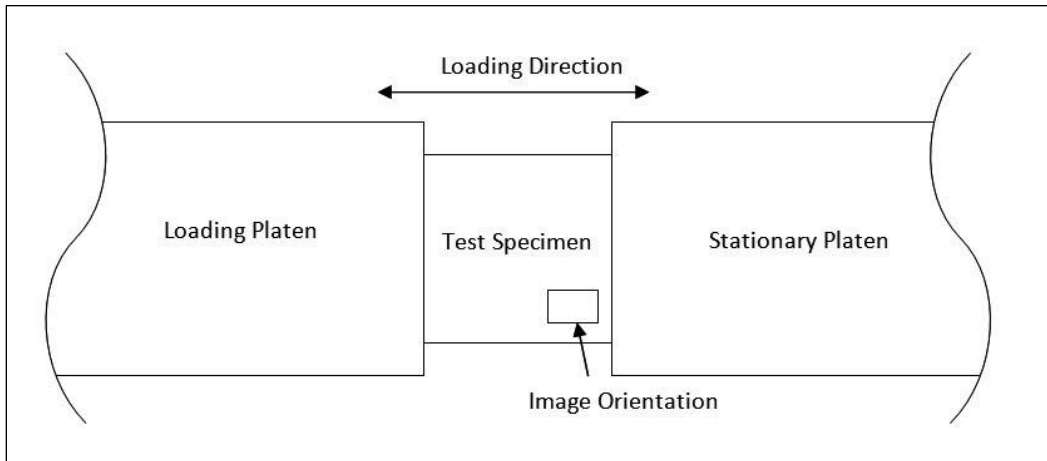
Figure 5. Schematic of testing orientation for quasi-static and dynamic compression.

3.3.1 Nano-Tungsten

A brittle fracture mechanism was observed in each of the nW compression tests. Each test registered strengths between 1.6–2.4 GPa as shown in figure 6 with brittle fracture occurring around the yield point. The hardness value of 5.9 GPa corresponds nicely with these results. In SHB compression testing, brittle fracture initiated at the surface of the specimen near the loading platen as shown in figure 7. Many of the dynamic and quasi-static compression samples failed catastrophically into a coarse dust. The observed fracture surface shows that intergranular fracture is the primary mode of failure. Nano-pores are clearly visible throughout the microstructure of the fractured surface.
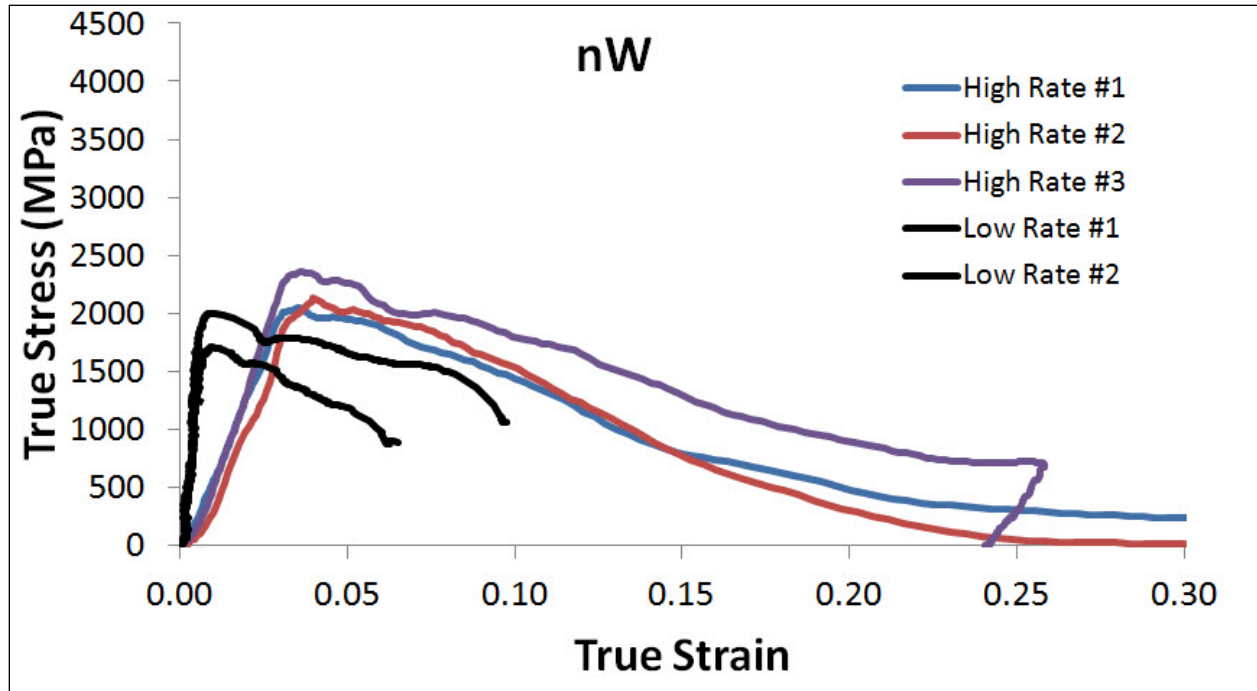
Figure 6. Quasi-static and dynamic compression test curves for nominally pure nano-structured tungsten sample. Low-rate tests failed into several pieces, high-rate compression tests fractured into coarse dust.
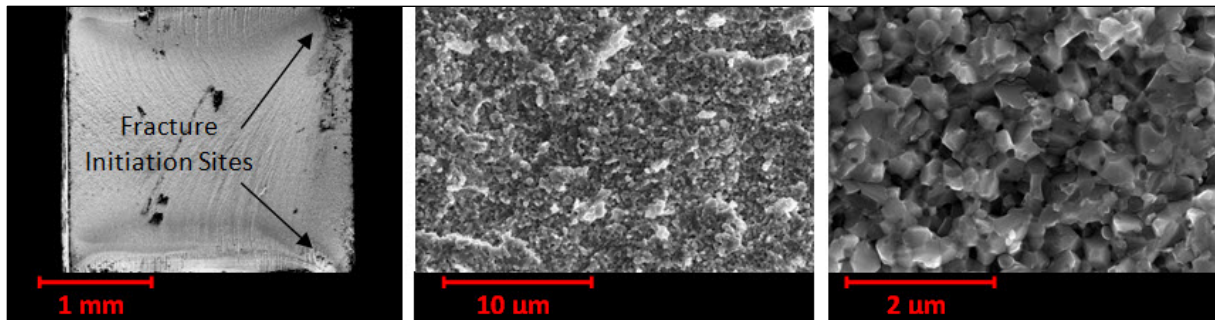
Figure 7. Fracture surface of nW SHB test specimens

3.3.2 Nano-Tungsten with Boron

The nano-tungsten sample with boron additions (nW-B) had the highest hardness and smallest grain size of any of the specimens tested; however there was significant variability in the compressive strength of each specimen. Each of the quasi-static compression tests failed at extremely low stresses and it was discovered that surface micro-cracking may have played a role in this premature failure. Dynamic compression test samples varied in strength from 2 to 4.2 GPa as shown in figure 8. Each sample failed catastrophically before any plastic deformation was realized and turned into a coarse sand. Figure 9 shows that the fracture surface of these specimens shows that failure is primarily transgranular in nature, although some intergranular failure is also noted. Significant nano-porosity appears throughout the fracture surface.

9
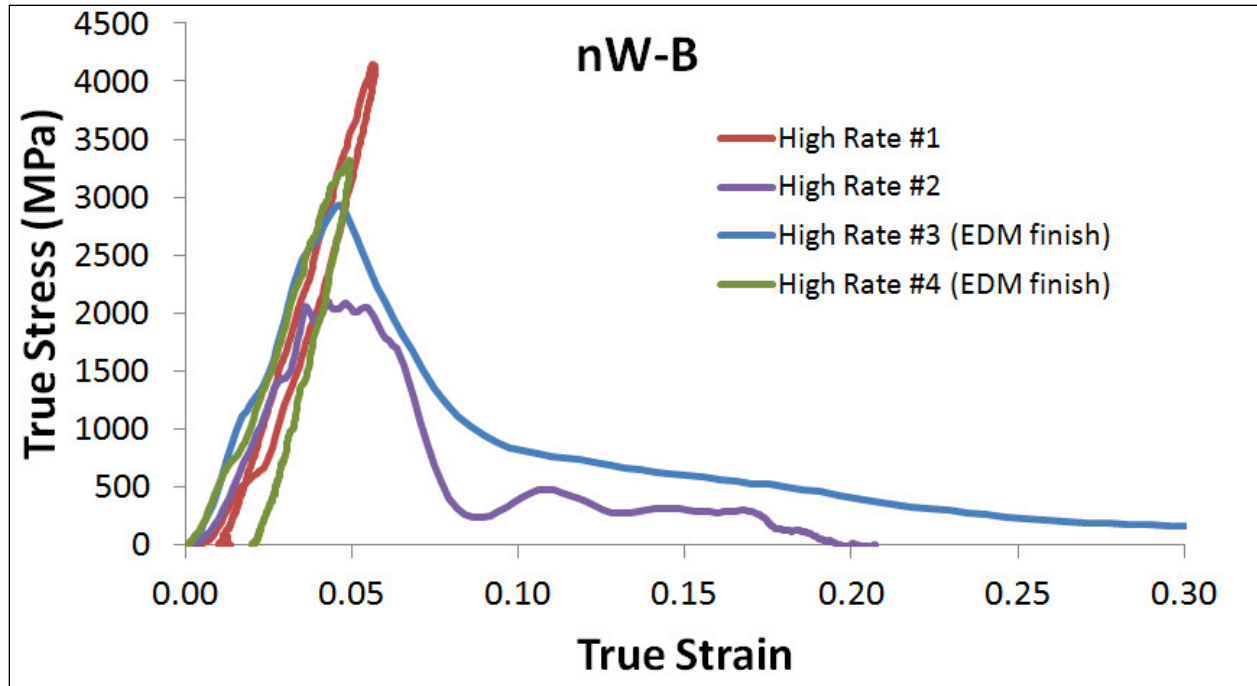
Figure 8. Dynamic compression test curves for nano-tungsten samples with boron additions. Low-rate tests failed at very low strain and are not shown above. High rate #1 failed into two large pieces with fracture propagating parallel to the loading direction. All other samples failed into several coarse pieces.
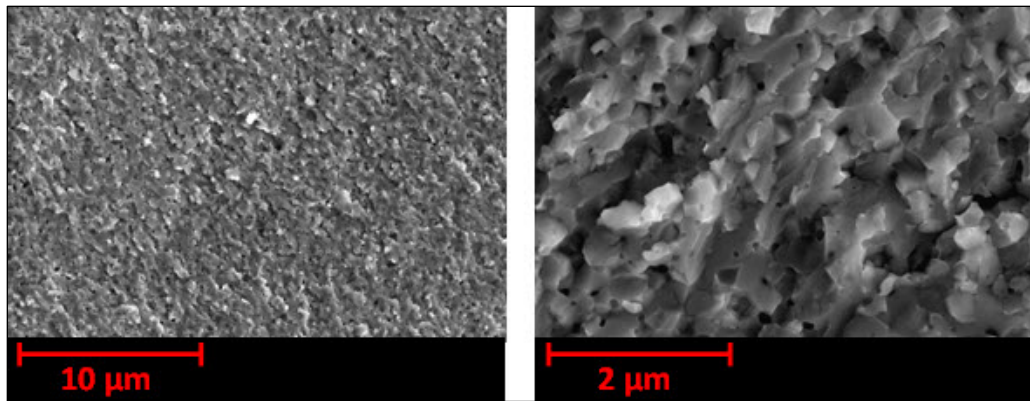
Figure 9. Fracture surface of nW-B SHB test specimens.

3.3.3 Nano-Tungsten with Bi-modal Distribution

The nano-tungsten with a bi-modal (nW-Bi Modal) distribution demonstrated a slightly higher strength and hardness than the conventional nanotungsten material with strengths ranging from 2.5–3.0 GPa as shown in figure 10. Compression test samples failed catastrophically without achieving any noticeable plastic deformation and the specimens were collected as a coarse dust. Fracture surfaces show many regions of large porosity and the failure mode appears to be intergranular throughout the entire nano-tungsten matrix. A significant amount of porosity was localized around the coarse particles, but the failure mode appeared to be predominantly transgranular for each of these coarse platelets indicating strong cohesion between the coarse

10

grains and the nano-structured matrix. SEM images of the nW-Bi Modal sample are shown in figure 11.
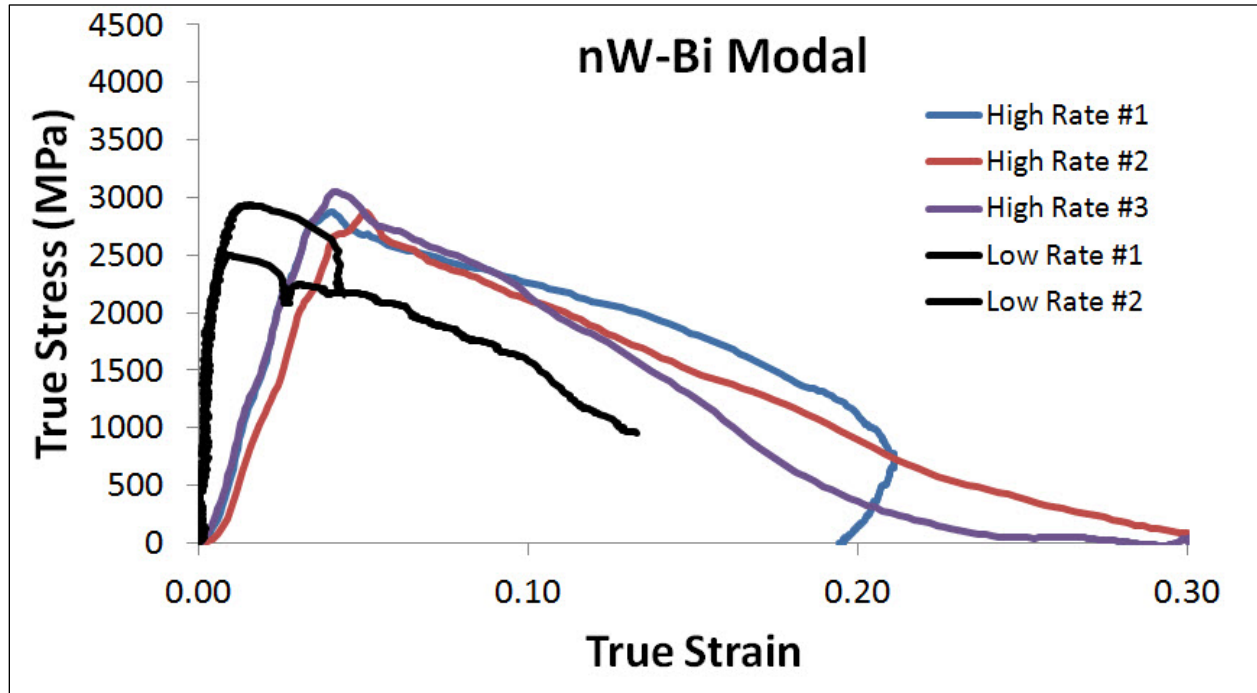
Figure 10. Quasi-static and dynamic compression test curves for nano-tungsten with coarse grain additions tungsten sample. Each specimen failed into a coarse dust.
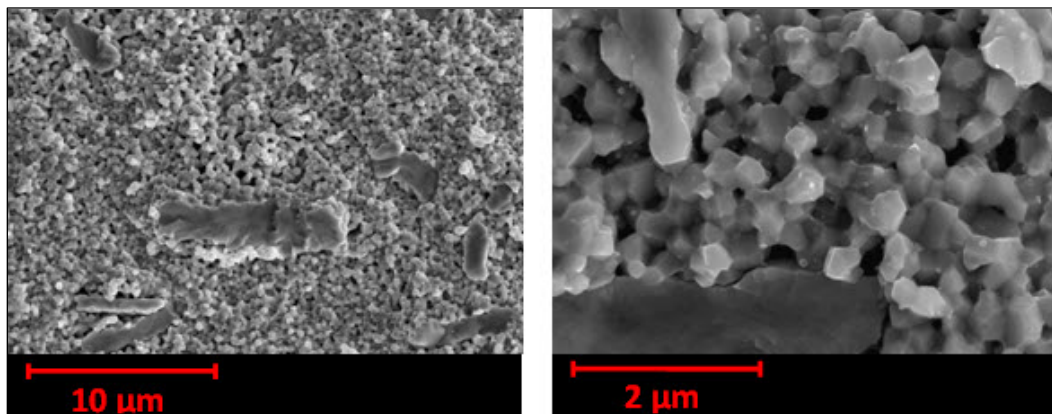
Figure 11. Fracture surface of nW-Bi Modal SHB test specimens.

3.3.4 Nano-Tungsten with 5% Rhenium

The nW-5Re sample had strengths ranging from 2.5–3 GPa in compression and demonstrated strain softening behavior in each of the mechanical tests as shown in figure 12. With a hardness value of 6.38 GPa, the nW-5Re samples were the softest rhenium containing samples tested. While each of the samples showed signs of shear localization, most of the samples ultimately experienced catastrophic brittle failure and fractured into several large pieces. Some of the compression test samples were polished with alumina to a 1-µm surface finish, while other

samples were tested with their original EDM surface finish. There did not appear to be any correlation between surface finish and ductility in any of these samples. Figure 13 shows SEM micrographs of a sample tested at high strain rates.
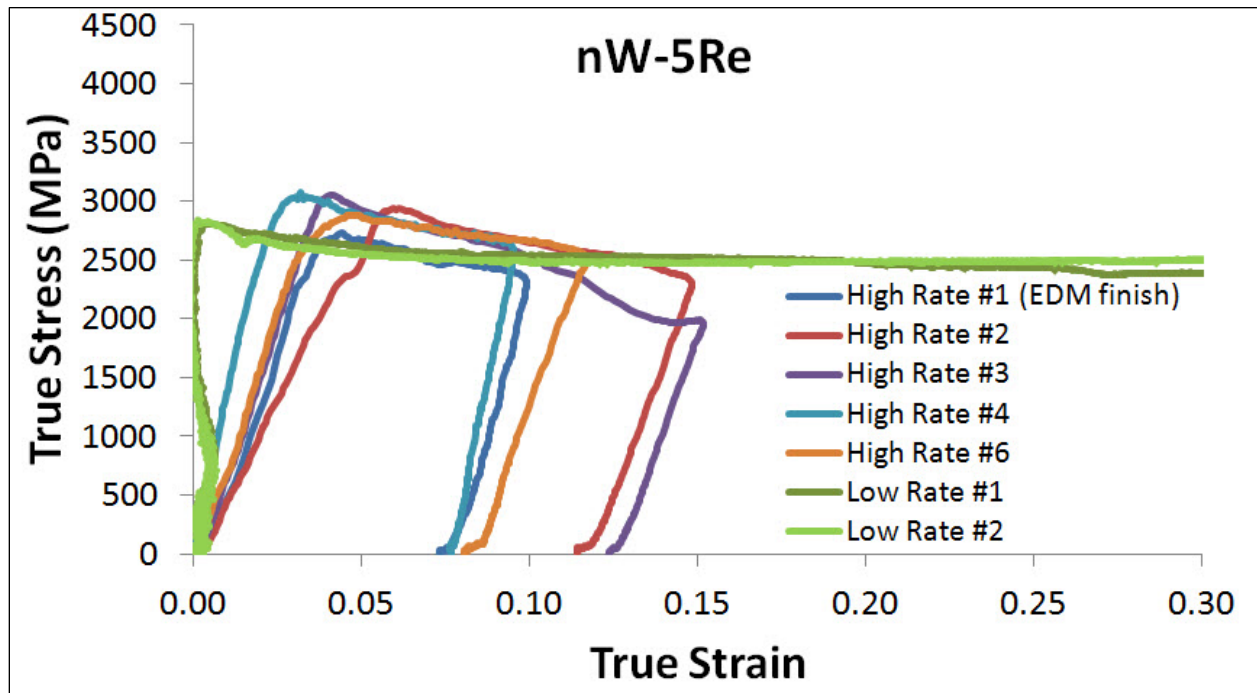
Figure 12. Quasi-static and dynamic compression test curves for nW-5Re. High-rate samples predominantly failed catastrophically into several large pieces; however this fracture was not shown in the in-situ test images acquired during loading and may have initiated as a result of the rebounding and second loading of the SHB. Low-rate samples did not fail catastrophically.
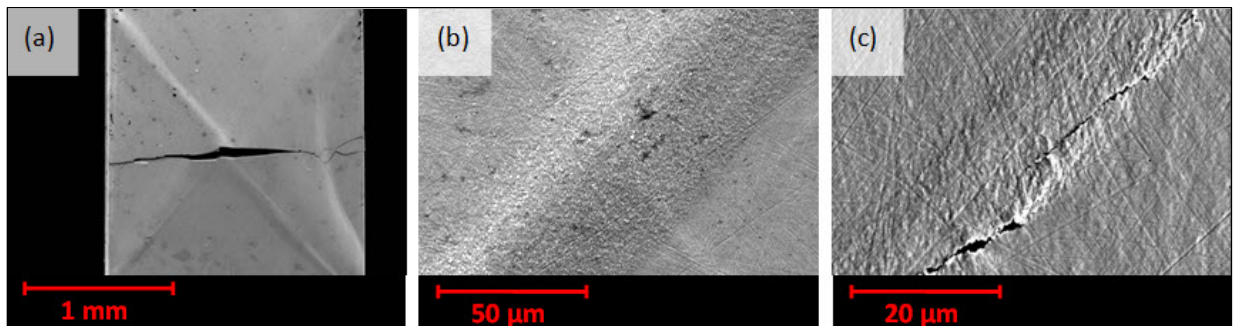
Figure 13. Surface of nW-5Re SHB compression test samples post mortem. (a) Macroscopic view of test specimen. (b) High magnification image of shear localization appearing at 45° to the loading direction. (c) High magnification image of combined shear localization and fracture failure mechanisms.

The nW-5Re sample clearly demonstrated brittle fracture in addition to shear localization. Major cracking occurred parallel to the loading front and additional micro-cracks occurred along the edge of shear bands at an angle of 45° to the loading direction. It is unclear whether these cracks in high strain rate specimens occurred during initial loading of the specimen as stress strain data shows that the specimen was intact during the unloading cycle. Figure 14 shows images of a

nW-5Re sample forming shear bands during SHB testing. The tested sample does not show any signs of brittle fracture during the initial compression and the stress-strain curve indicates that the sample unloads elastically.
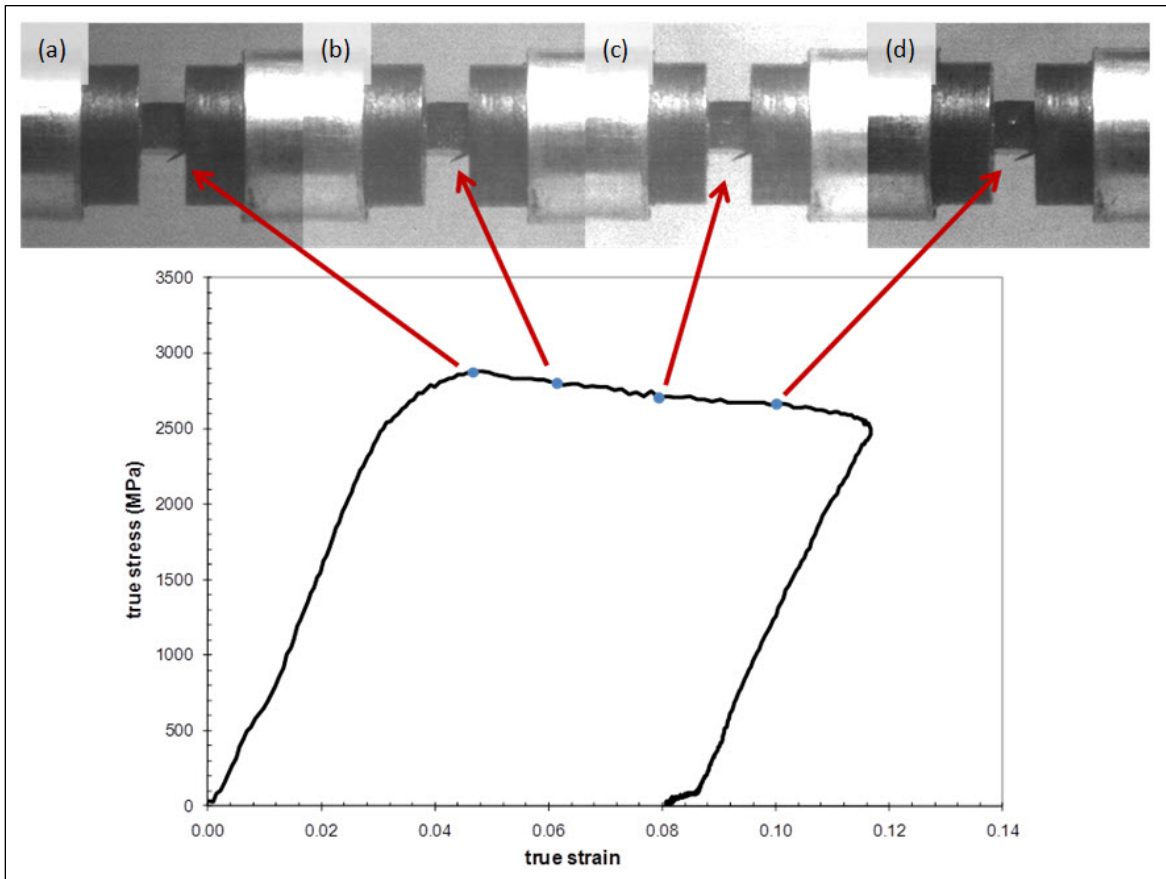
Figure 14. In-situ footage of shear band formation in nW-5Re. Deformation bands at 45° to the loading direction are visible in image (c) and (d). The stress-strain curve shows the same elastic response during the loading and unloading curve.

While shear band formation was clearly visible on the surface of the specimen, sectioning and polishing the samples after testing indicated that there was a fairly small difference between microstructures inside and outside of the heavily deformed region. Figure 15 shows the polished surface of the specimen outside and inside of the region of shear localization. The localized region shows a more elongated pore structure as a result of deformation. Also, the contrast between grains in the backscatter electron micrograph is visibly reduced as a result of deformation and crystal disorientation within grains.
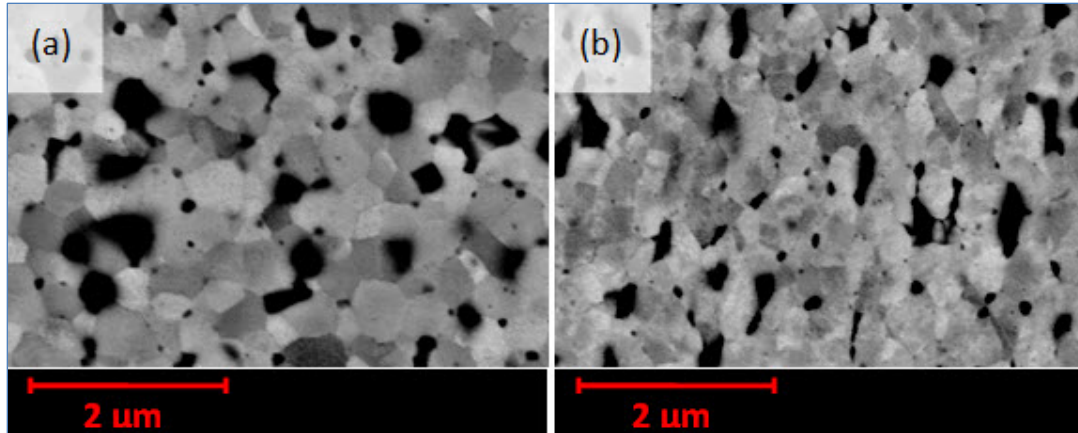
Figure 15. BSE images of a polished post mortem nW-5Re sample. (a) Area outside of localization region, (b) area inside of localization region.

Quasi-static compression testing also resulted in shear localization. The number of distinct shear bands was significantly greater than the SHB compression samples and the orientation of the shear bands varied as a result of the high degree of strain achieved in the quasi-static compression tests. Cracking was observed parallel to the loading direction and along shear bands in the same manner observed in the dynamic test specimens. Figure 16 shows images of the localization and cracking observed in the low rate nW-5Re test samples.
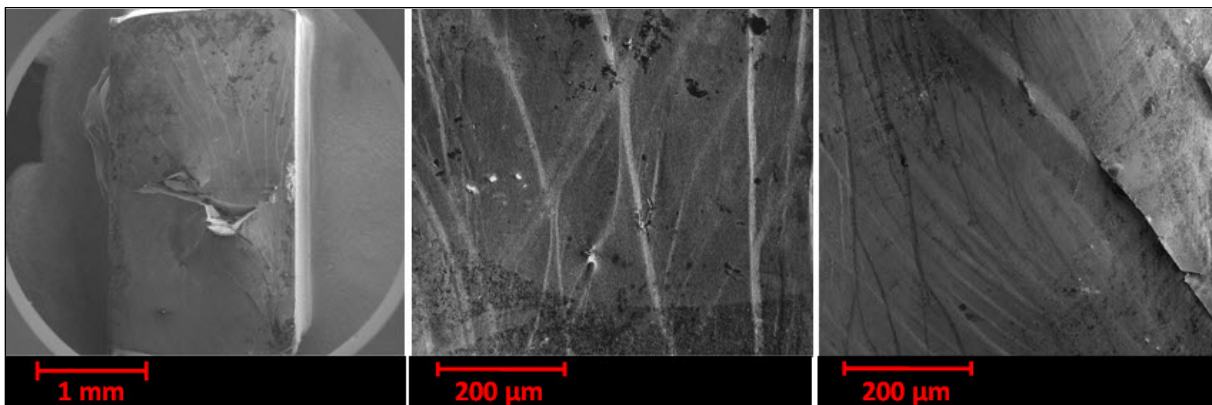
Figure 16. SEM images of quasi-static compression test specimens.

3.3.5 Nano-Tungsten with 10% Rhenium

The sample containing 10 weight-percent rhenium (nW-10Re) had quasi-static and dynamic strengths above 3 GPa as shown in figure 17 and demonstrated localization in each of the compression tests regardless of strain rate. Dynamic compression only resulted in a plastic strain of only 3%, but this strain was sufficient to induce definitive shear banding in the specimen. Quasi-static compression tests were carried out to nearly 30% strain without catastrophic failure. Each compression tested sample was polished to a 1-µm surface finish prior to testing. The hardness of the nW-10Re sample registered at 7.42 GPa. Post mortem images of the dynamic compression sample are shown in figure 18.
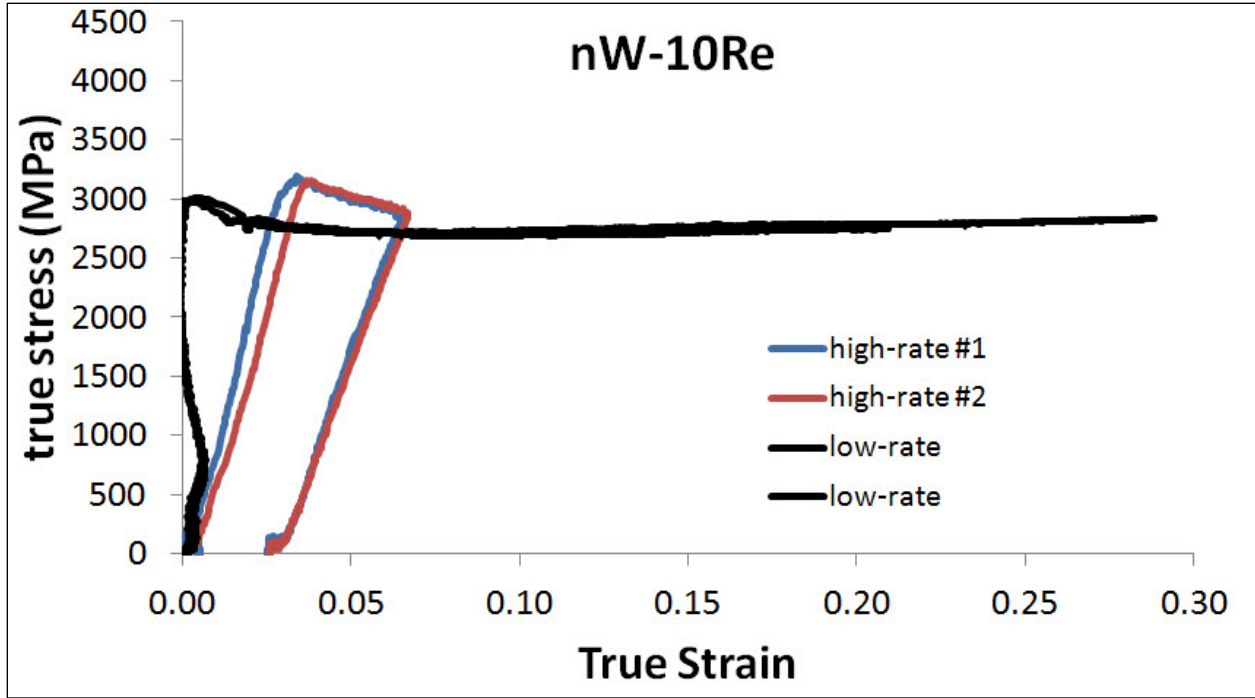
Figure 17. Quasi-static and dynamic compression test curves for nW-10Re. High-rate #1 fractured at 45° to the loading direction and the two halves continued to be compressed. High-rate #2 demonstrated localization at 45° to the loading direction but remained intact throughout the test.
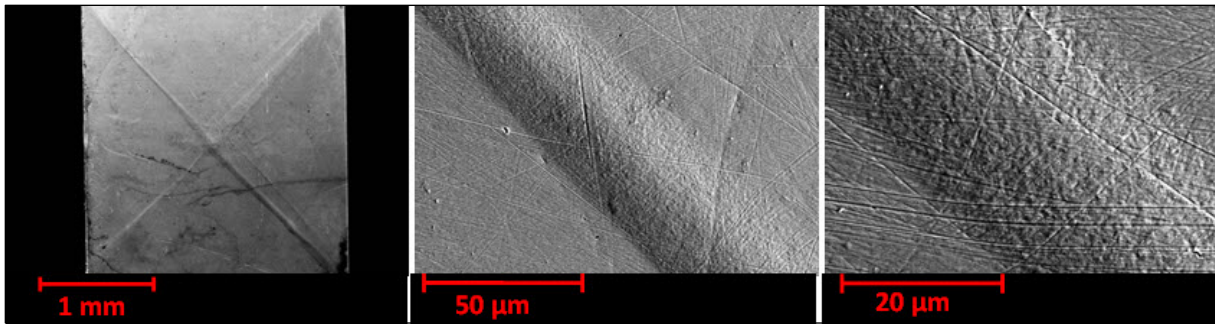
Figure 18. Post mortem images of SHB compression test samples with clear evidence of shear localization at 45° to the loading direction.

Images of shear localization were acquired during dynamic testing of the nW-10Re sample. Although the sample was only tested to ~3% plastic strain, the specimen showed clear evidence of shear localization in addition to strain softening during the SHB compression test as shown in figure 19. Each of the compression test samples remained intact after testing.
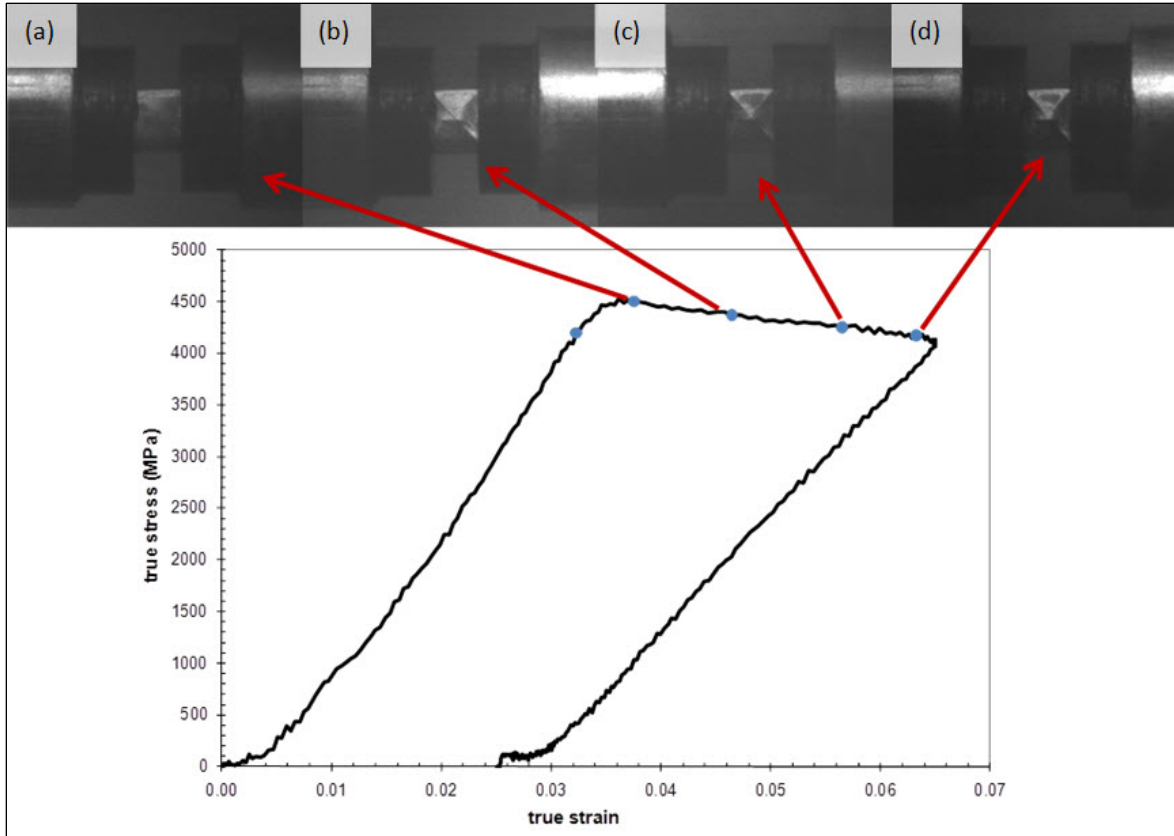
Figure 19. In-situ imaging of shear band formation in nW-10Re test samples during SHB compression testing. Evidence of shear band formation appears immediately after the yield point in image (b). Additional strain increases the visibility of the initial shear band and kicks off an orthogonal band as shown in image (d).

Samples tested at quasi-static compression rates also exhibited shear localization as shown in figure 20, though the regions of shear banding were more diffuse and varied slightly from the conventional 45° angle to the loading direction. This may have been a result of high strains achieved (>30%) in quasi-static compression. Some minor cracking occurred parallel to the loading direction; however, there were no observed cracks along the length of the shear bands.
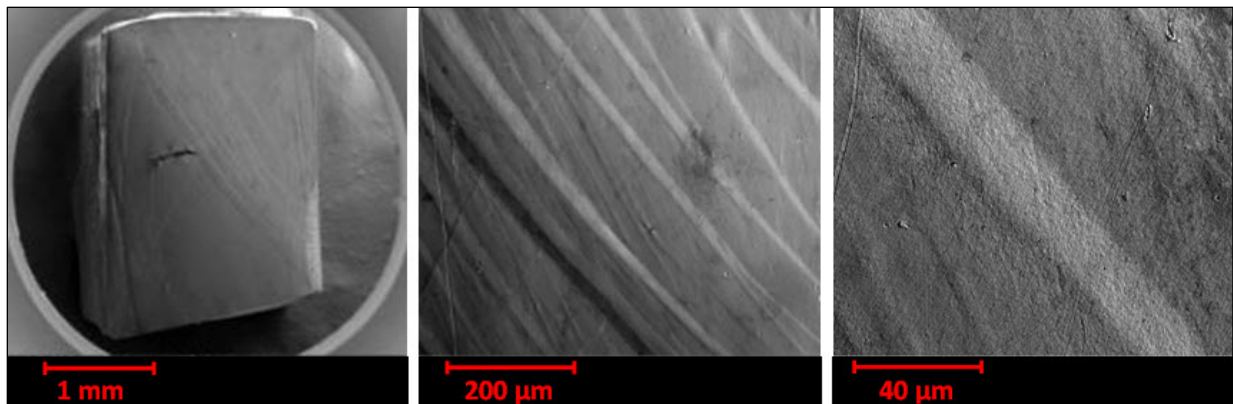
Figure 20. Images of nW-10Re compression specimens tested at quasi-static rates.

16

3.3.6 Nano-Tungsten with 25% Rhenium

Nano-tungsten samples with 25 weight-percent rhenium (nW-25Re) showed compressive strengths on the order of 2.5 GPa in quasi-static and dynamic testing as shown in figure 21. These high rhenium content samples had a hardness of 7.22 GPa. All of the samples showed a high degree of ductility in quasi-static and dynamic compression tests, achieving greater than 25% strain without fracture. One of the dynamic test samples was loaded multiple times without catastrophic failure. Unfortunately, none of the dynamic test specimens were recovered even though they survived testing without fracture.
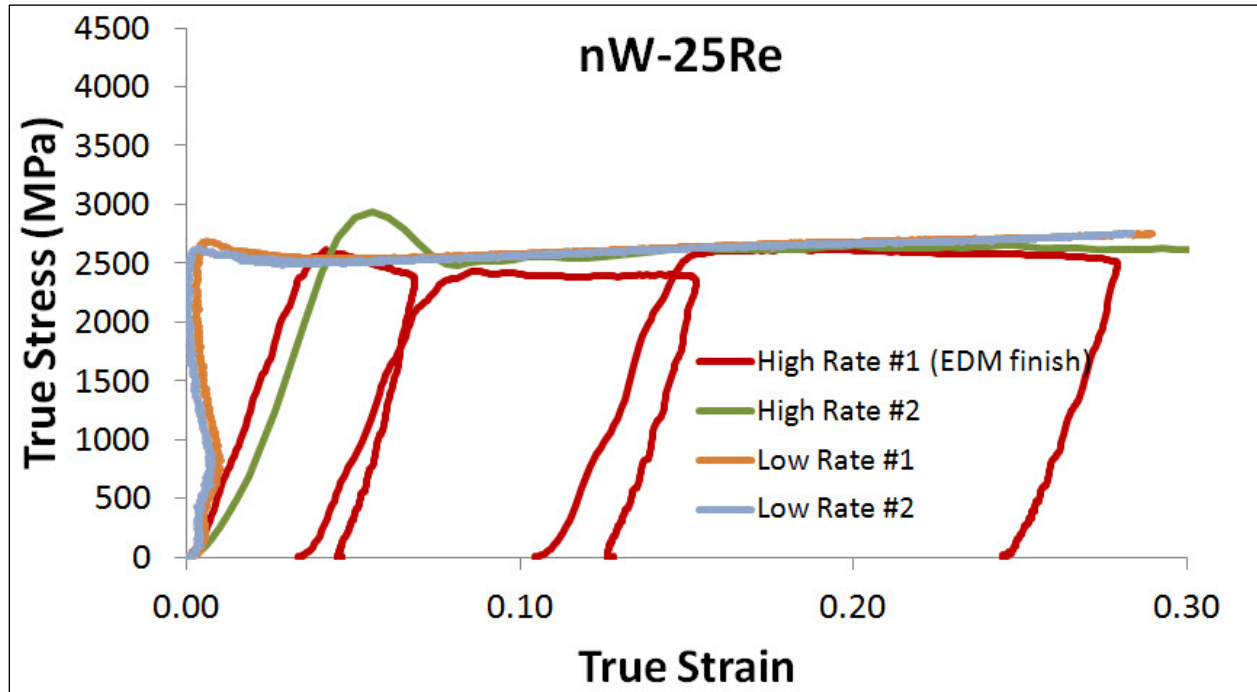
Figure 21. Quasi-static and dynamic compression test curves for nW-25Re. All specimens remained intact throughout the entire test; high-rate #1 was loaded and unloaded three separate times.

Quasi-static compression samples showed diffuse shear banding similar to other rhenium containing samples, though there were no signs of partial cracking in any of these specimens. Shear band direction varied slightly from the conventional 45° to the loading direction, which is likely a result of the significant plastic deformation observed in each specimen. Shear bands observed perpendicular to the loading direction are the result of shear bands observed on orthogonal surfaces as shown in figure 22.
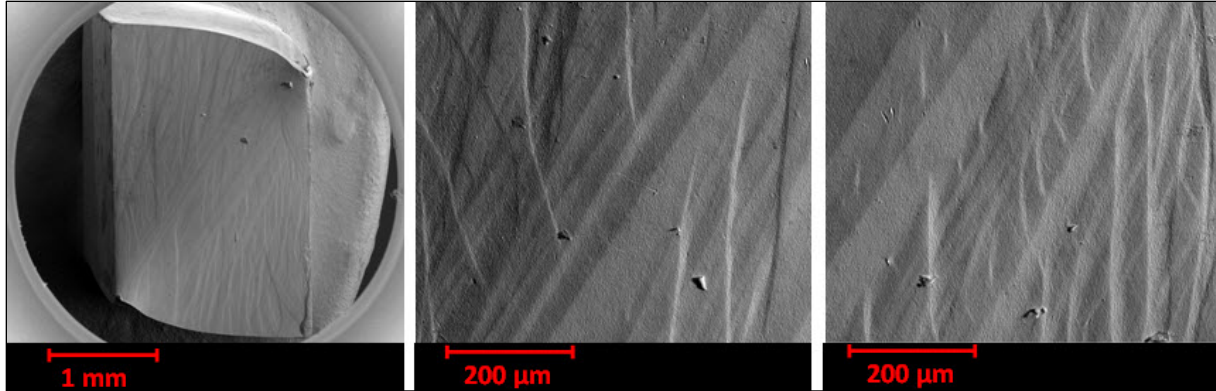
Figure 22. Images of nW-25Re compression specimens tested at quasi-static rates.

4. Summary of Results

Each of the samples tested had an ultra-fine grained microstructure (<500 nm) and a density greater than 17.8 cm^3. For compression test specimens, shear localization occurred in each of the samples containing rhenium, which is presumably a result of the enhanced ductility in these samples. Shear localization occurred regardless of strain rate indicating that the deformation mechanism is not the same as the adiabatic shear banding observed in depleted uranium. Microhardness testing indicated that the boron containing sample had a higher propensity to shear localize than any of the other specimens. However, this material did not have sufficient ductility to observe shear banding in a compression event. The grain sizes in the nW and nW-Bi Modal samples were significantly larger than the other compositions and may have inhibited shear band formation. A table summarizing the material properties and the results of mechanical testing is shown in table 1.

Table 1. Properties of nano-tungsten samples tested.

Deformation Mechanism	Sample ID	Macro Defects	Micro Defects	Surface Finish	Grain Size (nm)	Immersion Density (cm^3)	Immersion % Theo. Density (%)	Hardness (GPa)
No Shear Localization	nW	Possible Cracks	Large grains. Some areas of large porosity surrounded by coarse grains.	Polished	435	18.4	95.2%	5.92
	nW-B	Cracks Present	None	Some Polished Some EDM	163	18.5	95.9%	10.29
	nW-Bi Modal	No Visible Defects	High porosity regions surrounding coarse elongated particles.	Polished	421	17.8	92.2%	6.07
Shear Localization	nW-5Re	No Visible Defects	None	Some Polished Some EDM	321	18.3	94.7%	6.38
	nW-10Re	No Visible Defects	Some areas of large pores surrounded by coarse grains.	Polished	285	18.6	96.6%	7.42
	nW-25Re	No Visible Defects	Possible segregation of sigma phase present in sample.	Some Polished Some EDM	222	18.6	96.4%	7.22

5. Discussion

The tendency for nanomaterials to shear localize is strongly dependent on the underlying microstructure of the specimen. While previous research studies have indicated that there is a critical grain size necessary to achieve localization, there are many other microstructural and material properties which must be considered to determine whether deformation will occur by brittle fracture or shear localization. The presence of cracking and macro-defects prior to deformation is a strong sign that the material will behave in a brittle fashion as these sites create stress risers once a load is applied to the sample. It would be expected that surface finish would also play a critical role in the deformation properties, especially in the case of EDM surfaces where there is significant oxidation and micro-cracking at the surface; however, the tests conducted in this study showed little effect from surface finish.

Micro-defects such as porosity and phase segregation will also play a critical role in the deformation properties of each sample. While each material exhibits some degree of nano-porosity as a result of incomplete consolidation, there is some variation with respect to the size, uniformity and contiguity of porosity in each sample. Sample nW-B had the finest pores with the most uniform distribution, while nW had the largest average pore diameter and exhibited some degree of pore contiguity. Each of the remaining samples had similar pore sizes; however nW-Bi Modal did show that larger pores tended to concentrate around the coarse tungsten phase. Some phase segregation was noted in the nW-25Re samples and XRD analysis was able to identify the presence of the brittle σ (WRe) phase. The presence of sigma phase did not appear to have any negative influence on the mechanical properties of the sample. Furthermore, the presence of a di-tungsten boride (W_2B) phase was not detected in the nW-B sample, but the low concentration of boron may have made this phase undetectable by XRD techniques.

Although there was some significant variation in microstructure, hardness values were fairly consistent for each of the recorded specimens with the exception of the nW-B sample. This deviation is likely a result of the incredibly fine grain size (163 nm). Strain localization was observed around hardness indents in the nW-B samples; however, the samples did not have sufficient ductility to show strain localization in bulk compression tests. Each of the rhenium containing samples localized during compression testing under both quasi-static and dynamic loading conditions.

6. Conclusions

It was determined that hardness tests were not sufficient for predicting localization in bulk compression testing. When localization occurred in quasi-static and dynamic test specimens, it was limited to samples that showed appreciable ductility before failure. For the compositions that did exhibit localization in compression testing, the fact that this localization occurred in both the quasi-static and dynamic tests is further confirmation that this localization is a result of the geometric mechanism that is typical of ultrafine grained structures and not the result of an adiabatic softening mechanism. This mechanism requires some grain boundary sliding and reorientation prior to the initiation of a shear band and is therefore strongly dependent on the overall ductility of the material. In particular, this shear banding mechanism relies on some compliance in the grain boundary and will not occur in samples that are prone to brittle intergranular fracture.

This research demonstrated the first reliable shear localization in a high density (>18 cm^3) tungsten based alloy produced directly from powder metallurgy processes. The ability to shear localize was determined to be a function of the grain size of the material, as supported by previous research, as well as the ductility of the sample. Ductilization of nano-tungsten was accomplished through the addition of conventional alloy additions that demonstrated their ability to lower the ductile to brittle transition temperature of coarse grained tungsten. While rhenium additions were most effective in ductilizing nano-tungsten, the full benefit of boron additions and bi-modal distributions was not realized as a result of the presence of micro-defects and residual porosity that could have been minimized through careful process control. While the addition of rhenium is simple and effective for ductilizing tungsten in this proof-of-principle experiment, rhenium is an extremely expensive alloy addition that would limit use to all but a few niche applications. Alternative ductilization methods (i.e., deformation processing) must be used to improve the deformation behavior of nano-structured tungsten for KEP applications.

7. References

1. Magness, L. S.; Farrand, T. G. Deformation Behavior and Its Relationship to the Penetration Performance of High-Density Kinetic Energy Penetrator Materials. *Proceedings of the 1990 Army Science Conference,* 1990; 149–165.

2. Magness, L. S. High Strain Rate Deformation Behaviors of Kinetic Energy Penetrator Materials During Ballistic Impact. *Mechanics of Materials* **1994,** *17*, 147–154.

3. Magness, L.; Kecskes, L.; Chung, M.; Kapoor, D.; Biancianello, F.; Ridder, S. Behavior and Performance of Amorphous and Nanocrystalline Metals in Ballistic Impacts. *Proceedings from the 19th International Symposium of Ballistics*, Interlaken, Switzerland, May 2001.

4. Leonard, W.; Magness, L. S.; Dowding, R. J.; Trogolo, J.; Chung, M.; Kapoor, D. Ballistic Performance of Oriented Columnar-Grained Tungsten Polycrystals. *Tungsten and Refractory Metals* **1995**, 103–114.

5. Leonard, W.; Magness, L. S. *The Terminal Ballistic Performance of Microstructural Oriented Tungsten Heavy Alloy Penetrators*; ARL-TR-881; U.S. Army Research Laboratory: Aberdeen Proving Ground, MD, October 1995.

6. Li, H.; Subhash, G.; Kecskes, L. J.; Dowding, R. J. Mechanical Behavior of Tungsten Preform Reinforced Bulk Metallic Glass Composites. *Materials Science and Engineering: A* **2005**, *403,* 134–143.

7. Ramesh, K. T. *Nanomaterials: Mechanics and Mechanisms*; Springer Science+Business Media, New York, NY, 2009, 179–213.

8. Meyers, M. A.; Mishra, A.; Benson, D. J. Mechanical Properties of Nanocrystalline Materials. *Progress in Materials Science* **2006**, *51*, 427–556.

9. Wright, T. W. *The physics and mathematics of adiabatic shear bands*, Cambridge University Press: Cambridge, UK, 2002.

10. Wei, Q.; Jiao, T.; Ramesh, K. T.; Ma, E.; Kecskes, L.; Magness, L.; Dowding, R.; Kazykhanov, V.; Valiev, R. Mechanical Behavior and Dynamic Failure of High-Strength Ultrafine Grained Tungsten Under Uniaxial Compression. *Acta Materialia* **2006**, *54*, 77–87.

11. Wei, Q.; Zhang, H. T.; Schuster, B. E.; Ramesh, K. T.; Valiev, R. Z.; Kecskes, L. J.; Dowding, R. J.; Magness, L.; Cho, K. Microstructure and Mechanical Properties of Super-Strong Nanocrystalline Tungsten Processed by High-Pressure Torsion. *Acta Materialia* **2006**, *54*, 4079–4089.

12. Wei, Q.; Ramesh, K.T.; Ma, E.; Kesckes, L. J.; Dowding, R. J.; Kazykhanov, V. U.; Valiev, R. Z. Plastic Flow Localization in Bulk Tungsten with Ultrafine Microstructure. *Applied Physics Letters* **2005**, *86*, 101907–101907.

13. Zhilyaev, A. P.; Nurislamova, G. V.; Kim, B. K.; Baro, M. D.; Szpunar, J. A.; Langdon, T. G. Experimental Parameters Influencing Grain Refinement and Microstructural Evolution During High-Pressure Torsion. *Acta Materialia* **2003**, *51*, 753–765.

14. Zhilyaev, A. P.; Langdon, T. G. Using High-Pressure Torsion for Metal Processing: Fundamentals and Applications. *Progress in Materials Science* **2008**, *53*, 893–979.

15. Butler, B.; Klier, E.; Kelly, M.; Gallagher, M. *Thermal Stability of Milled Nanocrystalline Tungsten Powders*; ARL-TR-5541; U.S. Army Research Laboratory: Aberdeen Proving Ground, MD, May 2011.

16. Coolidge, W. D. Ductile Tungsten, *Transactions of the American Institute of Electrical Engineers* **1910**, *29*, 961–965.

17. Raffo, P. L. Yielding and Fracture in Tungsten and Tungsten-Rhenium Alloys. *Journal of the Less Common Metals* **1969**, *17*, 133–149.

18. Stephens, J. R. Dislocation Structures in Single-Crystal Tungsten and Tungsten Alloys. *Metallurgical and Materials Transactions B* **1970**, *1*, 1293–1301.

19. Klopp, W. D.; Holden, F. C.; Jaffee, R. I. *Further Studies on Rhenium Alloying Effects in Molybdenum, Tungsten, and Chromium*, Battelle Memorial Inst., Columbus, Ohio, 1960.

20. Lassner, E.; Schubert, W. D. *Tungsten: Properties, Chemistry, Technology of the Element, Alloys, and Chemical Compounds*, Kluwer Academic and Plenum Publishers, New York, NY, 1999, 256.

21. Krasko, G. L. Effect of Impurities on the Electronic Structure of Grain Boundaries and Intergranular Cohesion in Tungsten. *International Journal of Refractory Metals and Hard Materials* **1994**, *12*, 251–260.

22. Grujicic, M.; Zhao, H.; Krasko, G. L. Atomistic Simulation of Σ3 (111) Grain Boundary Fracture in Tungsten Containing Various Impurities. *International Journal of Refractory Metals and Hard Materials* **1997**, *15*, 341–355.

23. Wang, Y.; Chen, M.; Zhou, F.; Ma, E. High Tensile Ductility in a Nanostructured Metal. *Nature* **2002**, *419*, 912–919.

24. Kolsky, H. An Investigation of the Mechanical Properties of Materials at Very High Rates of Loading. *Proceedings of the Physical Society: Section B*, **1949**, *62*, 676–700.

25. Ren, L.; Larson, M.; Gama, B.; Gillespie, J. *Wave Dispersion in Cylindrical Tubes: Applications to Hopkinson Pressure Bar Experimental Techniques*; ARL-CR-551, U.S. Army Research Laboratory: Aberdeen Proving Ground, MD, September 2004.

26. Follansbee, P.; Frantz, C. Wave Propagation in the Split Hopkinson Pressure Bar. *Journal of Engineering Materials and Technology* **1983**, *105,* 61–66.

27. Trelewicz, J. R.; Schuh, C. A. The Hall-Petch Breakdown in Nanocrystalline Metals: A Crossover to Glass-like Deformation. *Acta Materialia* **2007**, *55* (17), 5948–5958.

List of Symbols, Abbreviations, and Acronyms

ARL	U.S. Army Research Laboratory
ASB	adiabatic shear bands
BSE	backscatter electron
DBTT	ductile to brittle transition temperature
DU	depleted uranium
EDM	electrical discharge machine, machining (or machined)
HPT	high pressure torsion
HRSEM	high resolution scanning electron microscope
KEP	kinetic energy penetrator
MoS_2	molybdenum disulfide
nW	nano-tungsten
nW-10Re	nano-tungsten alloys with 10 weight-percent rhenium
nW-25Re	nano-tungsten alloys with 25 weight-percent rhenium
nW-5Re	nano-tungsten alloys with 5 weight-percent rhenium
nW-B	nano-tungsten with boron
nW-Bi Modal	nano-tungsten with bi-modal distribution
SEM	scanning electron microscope
SHB	Split Hopkinson Bar
UFG	ultrafine grained
W_2B	di-tungsten boride
XRD	x-ray diffraction

NO. OF COPIES	ORGANIZATION
1 (PDF only)	DEFENSE TECHNICAL INFORMATION CTR DTIC OCA 8725 JOHN J KINGMAN RD STE 0944 FORT BELVOIR VA 22060-6218
1	DIRECTOR US ARMY RESEARCH LAB IMAL HRA MAIL & RECORDS MGMT 2800 POWDER MILL RD ADELPHI MD 20783-1197
1	DIRECTOR US ARMY RESEARCH LAB RDRL CIO LL 2800 POWDER MILL RD ADELPHI MD 20783-1197
1	DIRECTOR US ARMY RESEARCH LAB RDRL CIO LT 2800 POWDER MILL RD ADELPHI MD 20783-1197
1	US ARMY RESEARCH OFFICE S MATHAUDHU BLDG 12211 RESEARCH TRIANGLE PARK NC 27709-2211
1	US ARMY ARDEC D KAPOOR AMSRD AAR AEE-P, BLDG 25 PICATINNY ARSENAL NJ 07806-5000

NO. OF COPIES	ORGANIZATION
	ABERDEEN PROVING GROUND
15	RDRL WM J MCCAULEY RDRL WMM J BEATTY R DOWDING RDRL WMM F B BUTLER (2 CPS) S GRENDAHL H MAUPIN E KLIER L KESKES K DARLING RDRL WML J NEWILL M ZOLTOSK RDRL WML H L MAGNESS B SCHUSTER RDRL WMP B D CASEM